

# Continuously tunable terahertz metamaterial employing magnetically actuated cantilevers

Burak Ozbey<sup>1</sup> and Ozgur Aktas<sup>1,\*</sup>

<sup>1</sup>Department of Electrical and Electronics Engineering, Bilkent University, Bilkent, Ankara, Turkey  
\*aktas@ee.bilkent.edu.tr

**Abstract:** Terahertz metamaterial structures that employ flexing microelectromechanical cantilevers for tuning the resonance frequency of an electric split-ring resonator are presented. The tuning cantilevers are coated with a magnetic thin-film and are actuated by an external magnetic field. The use of cantilevers enables continuous tuning of the resonance frequency over a large frequency range. The use of an externally applied magnetic field for actuation simplifies the metamaterial structure and its use for sensor or filter applications. A structure for minimizing the actuating field is derived. The dependence of the tunable bandwidth on frequency is discussed.

©2011 Optical Society of America

OCIS codes: (160.3918) Metamaterials; (070.4790) Spectrum Analysis; (040.1880) Detection

## References and links

1. V. G. Veselago, "The electrodynamics of substances with simultaneously negative values of  $\epsilon$  and  $\mu$ ," *Sov. Phys. Usp.* **10**(4), 509–514 (1968).
2. N. I. Zheludev, "Applied physics. The road ahead for metamaterials," *Science* **328**(5978), 582–583 (2010).
3. R. A. Shelby, D. R. Smith, and S. Schultz, "Experimental Verification of a Negative Index of Refraction," *Science* **292**(5514), 77–79 (2001).
4. J. B. Pendry, "Negative refraction makes a perfect lens," *Phys. Rev. Lett.* **85**(18), 3966–3969 (2000).
5. A. Grbic, and G. V. Eleftheriades, "Overcoming the diffraction limit with a planar left-handed transmission-line lens," *Phys. Rev. Lett.* **92**(11), 117403 (2004).
6. Z. Lu, S. Shi, C. A. Schuetz, and D. W. Prather, "Experimental demonstration of negative refraction imaging in both amplitude and phase," *Opt. Express* **13**(6), 2007–2012 (2005).
7. H. J. Lezec, J. A. Dionne, and H. A. Atwater, "Negative refraction at visible frequencies," *Science* **316**(5823), 430–432 (2007).
8. T. Taubner, D. Korobkin, Y. Urzhumov, G. Shvets, and R. Hillenbrand, "Near-field microscopy through a SiC superlens," *Science* **313**(5793), 1595 (2006).
9. N. Fang, H. Lee, C. Sun, and X. Zhang, "Sub-diffraction-limited optical imaging with a silver superlens," *Science* **308**(5721), 534–537 (2005).
10. D. Schurig, J. J. Mock, B. J. Justice, S. A. Cummer, J. B. Pendry, A. F. Starr, and D. R. Smith, "Metamaterial electromagnetic cloak at microwave frequencies," *Science* **314**(5801), 977–980 (2006).
11. N. Engheta, and R. W. Ziolkowski, *Metamaterials: Physics and Engineering Explorations* (Wiley Interscience, 2006).
12. C. M. Bingham, H. Tao, X. Liu, R. D. Averitt, X. Zhang, and W. J. Padilla, "Planar wallpaper group metamaterials for novel terahertz applications," *Opt. Express* **16**(23), 18565–18575 (2008).
13. W. Withayachumnankul, and D. Abbott, "Metamaterials in the Terahertz Regime," *IEEE Photon. J.* **1**(2), 99–118 (2009).
14. W. J. Padilla, M. T. Aronsson, C. Highstrete, M. Lee, A. J. Taylor, and R. D. Averitt, "Electrically resonant terahertz metamaterials: Theoretical and experimental investigations," *Phys. Rev. B* **75**(4), 041102 (2007).
15. S.-Y. Chiam, R. Singh, J. Gu, J. Han, W. Zhang, and A. A. Bettiol, "Increased frequency shifts in high aspect ratio terahertz split ring resonators," *Appl. Phys. Lett.* **94**(6), 064102 (2009).
16. I. A. I. Al-Naib, C. Jansen, and M. Koch, "High Q-factor metasurfaces based on miniaturized asymmetric single split resonators," *Appl. Phys. Lett.* **94**(15), 153505 (2009).
17. S. P. Micken, A. Menikh, H. B. Liu, C. A. Mannella, R. MacColl, D. Abbott, J. Munch, and X. C. Zhang, "Label-free bioaffinity detection using terahertz technology," *Phys. Med. Biol.* **47**(21), 3789–3795 (2002).
18. J. F. O'Hara, R. Singh, I. Brener, E. Smirnova, J. G. Han, A. J. Taylor, and W. L. Zhang, "Thin-film sensing with planar terahertz metamaterials: sensitivity and limitations," *Opt. Express* **16**(3), 1786–1795 (2008).
19. M. Nagel, P. H. Bolivar, M. Brucherseifer, H. Kurz, A. Bosserhoff, and R. Büttner, "Integrated THz technology for label-free genetic diagnostics," *Appl. Phys. Lett.* **80**(1), 154–156 (2002).
20. C. Debus, and P. H. Bolivar, "Frequency selective surfaces for high sensitivity terahertz sensing," *Appl. Phys. Lett.* **91**(18), 184102 (2007).

21. H. T. Chen, W. J. Padilla, J. M. O. Zide, A. C. Gossard, A. J. Taylor, and R. D. Averitt, "Active terahertz metamaterial devices," *Nature* **444**(7119), 597–600 (2006).
22. H. T. Chen, J. F. O'Hara, A. K. Azad, A. J. Taylor, R. D. Averitt, D. B. Shrekenhamer, and W. J. Padilla, "Experimental demonstration of frequency-agile terahertz metamaterials," *Nat. Photonics* **2**(5), 295–298 (2008).
23. H. T. Chen, W. J. Padilla, M. J. Cich, A. K. Azad, R. D. Averitt, and A. J. Taylor, "A metamaterial solid-state terahertz phase modulator," *Nat. Photonics* **3**(3), 148–151 (2009).
24. W. L. Chan, H. T. Chen, A. J. Taylor, I. Brener, M. J. Cich, and D. M. Mittleman, "A spatial light modulator for terahertz beams," *Appl. Phys. Lett.* **94**(21), 213511 (2009).
25. Y. H. Yuan, J. A. He, J. S. Liu, and J. Q. Yao, "Proposal of an electrically controlled terahertz switch based on liquid-crystal-filled dual-metallic grating structures," *Appl. Opt.* **49**(31), 6092–6097 (2010).
26. W. X. Huang, X. G. Yin, C. P. Huang, Q. J. Wang, T. F. Miao, and Y. Y. Zhu, "Optical switching of a metamaterial by temperature controlling," *Appl. Phys. Lett.* **96**(26), 261908 (2010).
27. M. J. Dicken, K. Aydin, I. M. Pryce, L. A. Sweatlock, E. M. Boyd, S. Walavalkar, J. Ma, and H. A. Atwater, "Frequency tunable near-infrared metamaterials based on VO<sub>2</sub> phase transition," *Opt. Express* **17**(20), 18330–18339 (2009).
28. B. B. Jin, C. H. Zhang, S. Engelbrecht, A. Pimenov, J. B. Wu, Q. Y. Xu, C. H. Cao, J. A. Chen, W. W. Xu, L. Kang, and P. H. Wu, "Low loss and magnetic field-tunable superconducting terahertz metamaterial," *Opt. Express* **18**(16), 17504–17509 (2010).
29. G. H. He, R. X. Wu, Y. Poo, and P. Chen, "Magnetically tunable double-negative material composed of ferrite-dielectric and metallic mesh," *J. Appl. Phys.* **107**(9), 093522–093527 (2010).
30. E. Ekmekci, K. Topalli, T. Akin, and G. Turhan-Sayan, "A tunable multi-band metamaterial design using micro-split SRR structures," *Opt. Express* **17**(18), 16046–16058 (2009).
31. G.T.A. Kovacs, *Micromachined Transducers Sourcebook* (McGraw-Hill 1998).
32. C. Liu, and Y. W. Li, "Micromachined magnetic actuators using electroplated permalloy," *IEEE Trans. Magn.* **35**(3), 1976–1985 (1999).
33. W. P. Taylor, O. Brand, and M. G. Allen, "Fully integrated magnetically actuated micromachined relays," *J. Microelectromech. Syst.* **7**(2), 181–191 (1998).
34. Y. H. Zhang, G. F. Ding, H. Wang, S. Fu, and B. C. Cai, "Low-stress permalloy for magnetic MEMS switches," *IEEE T. Magn.* **42**(1), 51–55 (2006).
35. S. Guan, and B. J. Nelson, "Electrodeposition of low residual stress CoNiMnP hard magnetic thin films for magnetic MEMS actuators," *J. Magn. Magn. Mater.* **292**, 49–58 (2005).
36. D. P. Arnold, and N. G. Wang, "Permanent Magnets for MEMS," *J. Microelectromech. Syst.* **18**(6), 1255–1266 (2009).
37. Computer Simulation Technology, <http://www.cst.com>
38. H. T. Chen, J. F. O'Hara, A. J. Taylor, R. D. Averitt, C. Highstrete, M. Lee, and W. J. Padilla, "Complementary planar terahertz metamaterials," *Opt. Express* **15**(3), 1084–1095 (2007).
39. F.P. Beer, E.R. Johnston Jr., J.T. DeWolf, D. Mazurek, *Mechanics of Materials* (McGraw-Hill 2009).
40. W. N. Sharpe, "Mechanical properties of MEMS materials," in *Proceedings of IEEE Semiconductor Device Research Symposium* (IEEE 2001), pp. 416–417.
41. A. K. Azad, A. J. Taylor, E. Smirnova, and J. F. O'Hara, "Characterization and analysis of terahertz metamaterials based on rectangular split-ring resonators," *Appl. Phys. Lett.* **92**(1), 011119–011193 (2008).

## 1. Introduction

Since their conceptual inception [1], most of the work on metamaterials has been motivated by the possibility to design their characteristics to exhibit behavior not usually possessed by natural materials [2]. Building on the publications presenting the initial designs and demonstrations [3–5], left-handed metamaterials that exhibit a negative index of refraction have been demonstrated in the microwave to visible region of the spectrum [6,7] and metamaterial structures that act as super-lenses have been demonstrated at microwave to millimeter-wave frequencies [5,8,9]. More recent work on metamaterials have concentrated on demonstration of interesting new phenomena such as cloaking [10] and application driven concepts such as active, nonlinear or tunable metamaterials [2,11].

The extension of the metamaterial research to terahertz frequencies has opened up possibilities for new applications whose technological importance has been a strong motivating factor [12–16]. Amongst these, the presence of resonances of several biological molecules in the terahertz range of frequencies makes sensors an especially important application area [17, 18]. Thus, structures that can be used as sensors and structures which can be used for spectroscopic analysis have been under intense development [18, 19].

Various affinity based approaches for adapting terahertz metamaterials for sensor devices have appeared in the literature [17–19]. These assume that the target molecule would be selectively bound to the metamaterial surface via a target specific binder. It was demonstrated that the binding of the target molecules at a high field position in the metamaterial structure

would provide the most sensitivity [20]. Based on the affinity probe principle, terahertz sensors that respond to a change in the dielectric constant or to a change in the absorption coefficient were demonstrated [18].

Tunable terahertz metamaterials have also received significant attention due to applications in both the sensing and spectroscopy field and optical communications area. Various methods for changing the resonant frequency of a metamaterial have been proposed and demonstrated [21–30]. While the existing designs of tunable metamaterials provide important functionality and possess certain advantages in each case, a terahertz metamaterial continuously tunable over a wide frequency range has not yet been demonstrated. The reports in the literature have either been tunable in discrete steps or tunable in a narrow band.

A metamaterial structure which can be tuned continuously in a wide frequency range can be advantageous for sensor and spectroscopy applications. Rather than designing a new metamaterial for each specific molecule to be sensed one common structure can be tuned to various frequencies and be used for all molecules of interest. Similarly, a tunable metamaterial can be used to sense for several materials at the same time. For spectroscopy applications a wideband tunable metamaterial will simplify the spectroscopy system and enable a wider range of frequencies to be investigated with the setup.

In this work, we present a novel approach that transforms the metamaterial structure to incorporate conventional microelectromechanical (MEMS) single-edge-fixed cantilevers into split-ring resonators [31]. The MEMS cantilevers used to tune the metamaterial are actuated by the force generated by an external field on the magnetic material coating the surface. Magnetic actuation of single end fixed cantilevers have been studied and demonstrated before [31–33]. Detailed experimental investigations have shown that the problem of curving of the cantilever under the residual stress of the magnetic layer can be addressed by depositing low stress materials by a variety of methods [34, 35]. Hard magnets with a high magnetization have also been investigated for application to actuation in MEMS systems [35, 36]. It is important to note that the fabrication of the structures proposed in this work rely only on conventional MEMS techniques. The mechanical properties of the proposed structures are analyzed and the suitability of the selected dimensions for proper operation is shown.

In this work, the electric split ring resonator metamaterial structure is modified in a way that will minimize the field magnitude required for actuation of the cantilever. Furthermore, the constraint that the stress in the cantilever will not exceed the bottom limit of the range of yield strength of the cantilever materials is also taken into account. Full-wave simulations show that the structure acts as an electric split-ring resonator (eSRR) and that the resonant frequency of the structures can be tuned over a large bandwidth. Through full-wave simulations, high quality factor structures are designed by modifying the design.

## 2. Simulation details

All the simulations in this work were performed by using the commercial time-domain simulator CST Microwave Studio [37]. The structures were defined from gold and resistive losses were taken into account during the simulations. In order to incorporate effect of dielectric constant of the substrate on the resonance characteristics, substrate was chosen to be 100  $\mu\text{m}$  thick loss-free quartz. Since low-loss substrates and dielectrics exist, the substrate losses and the losses in the dielectrics were ignored. Following the approach in the literature, the effect of the bare substrate on transmission was eliminated from the results by dividing the transmission of the metamaterial with the reference transmission of the bare substrate [38].

The periodic structure of the metamaterial was simulated by limiting the simulation domain to a single unit-cell and employing periodic boundary conditions in axis directions orthogonal to beam propagation. The structure was excited by using a plane wave incident from the substrate side. The transmitted field profile was probed at a position 400 micrometers away from the metamaterial surface. It was verified that moving the probe position further away does not make a significant difference in the measured field. The simulated unit-cell incorporated an empty space equal to 10  $\mu\text{m}$  beyond the eSRR structure itself to achieve a unit cell dimension 20  $\mu\text{m}$  larger than the dimensions of the eSRR structure.

This spacing is known to influence the properties of the metamaterial, but was not modified in the simulations performed in this work.

All simulations were performed as individual runs and the convergence of the results were checked by monitoring the change of energy in the domain and also by repeating the simulations by employing a finer mesh. From the mesh size dependent variation observed in the results, the accuracy of the resonance frequencies was estimated to be  $\pm 2$  percent.

### 3. Device structure

For terahertz frequencies, the electric split-ring resonator structure shown in Fig. 1a has been investigated previously. Theoretical and experimental investigations have shown that the eSRR structures exhibit several resonances, the lowest of which is due to the series inductor and capacitor that effectively exist in the structure. As shown in the Fig. 1a, the eSRR structure consists of two rings that share a common “split”. The current induced in the eSRR rings experience an inductive effect as it flows around the rings and a capacitive effect across the “split”. The resonance frequency of the eSRR can be adjusted by designing the length and area of the rings to adjust the inductive effect and by designing the split to adjust the capacitive effect. Previous demonstrations of tunable terahertz metamaterials have utilized the possibility to change the effective capacitance of the eSRR by changing the length or spacing of the split either by illumination, temperature change or applied bias [21–27].

The split in the eSRR structure can be replaced with a parallel plate capacitor without changing the operation and characteristics of the metamaterial. Such a structure and its transfer characteristics are compared to a classical eSRR in Fig. 1b. It is seen that the modified eSRR functions same as the classical eSRR.

The tunability of the modified eSRR can be achieved by replacing the parallel plate capacitor with a flexible cantilever beam with a height that can be changed. Such a structure is shown in Fig. 1c. With a cantilever beam, the series capacitance of the eSRR structure will come to depend on the bending of the beam. In order to change the bending of the cantilever beam a force will need to be applied to the structure. The deflection of the beam is known to be proportional to the cube of the length of the beam for a fixed force applied at the end of the beam [31]. Hence, the force needed to deflect the beam for a given displacement will be minimized if the beam is made as long as possible. In the eSRR structure, the cantilever length can be increased by moving the “split” from the center of the eSRR to the edge of the eSRR as shown in Fig. 1d. In Fig. 1c and Fig. 1d, the simulated transfer characteristics of these two modified eSRR structures are also shown.

The flexible cantilever concept shown in Fig. 1d can be utilized for an actual device by several methods. This paper investigates the use of magnetic actuation for the generation of the force needed to bend the cantilever. In the next section, the properties of magnetic actuation are investigated and the eSRR structure is modified to incorporate a magnetic layer of optimal dimensions. For the magnetic material, the saturation magnetization of permalloy ( $M=1$  Tesla) was used.

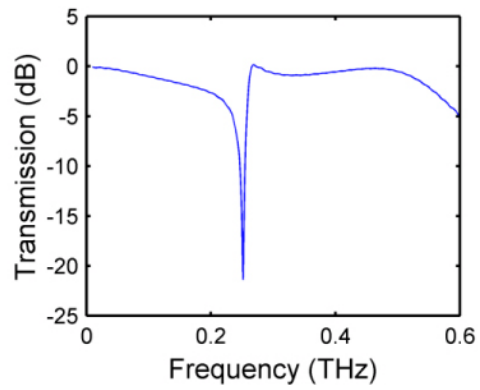


Fig. 1a. Structure and transfer characteristics of a classical eSRR. For the device simulated the sides are  $120\ \mu\text{m}$ , the arms are  $10\ \mu\text{m}$ , and the gap is  $2\ \mu\text{m}$ .

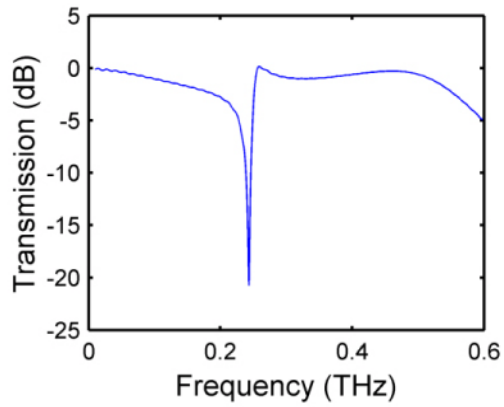


Fig. 1b. The structure and the transfer characteristics of an eSRR modified to incorporate a parallel plate capacitor. For the device simulated the sides are  $120\ \mu\text{m}$ , the arms are  $10\ \mu\text{m}$ , the height of the top plate from the bottom plate is  $3\ \mu\text{m}$ , and the bottom plate is  $60 \times 4\ \mu\text{m}$  square.

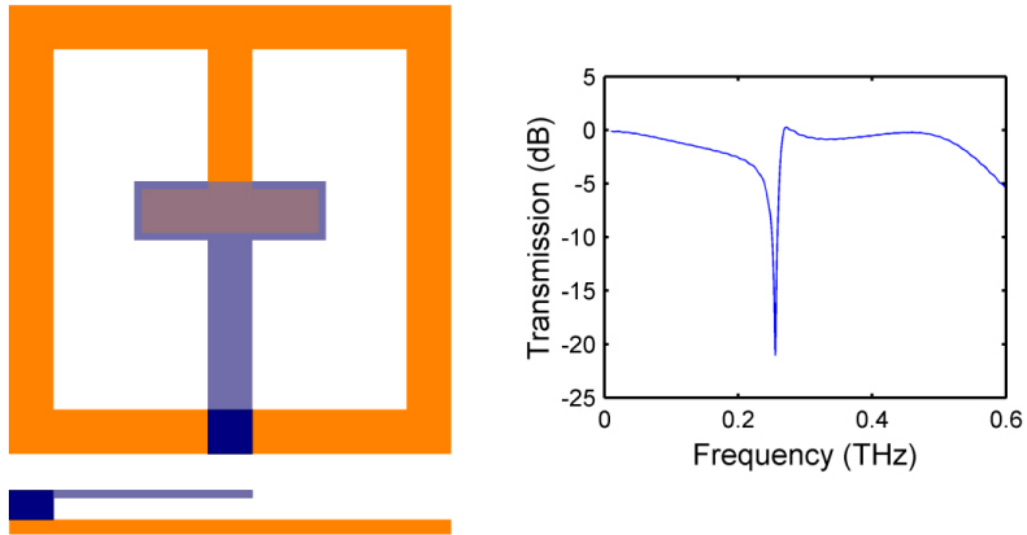


Fig. 1c. The structure and the transfer characteristics of an eSRR modified to incorporate a parallel plate capacitor with a flexing cantilever. For the device simulated the sides are  $120\ \mu\text{m}$ , the arms are  $10\ \mu\text{m}$ , the height of the top plate from the bottom plate is  $3\ \mu\text{m}$ , and the bottom plate is  $60 \times 4\ \mu\text{m}$  square.

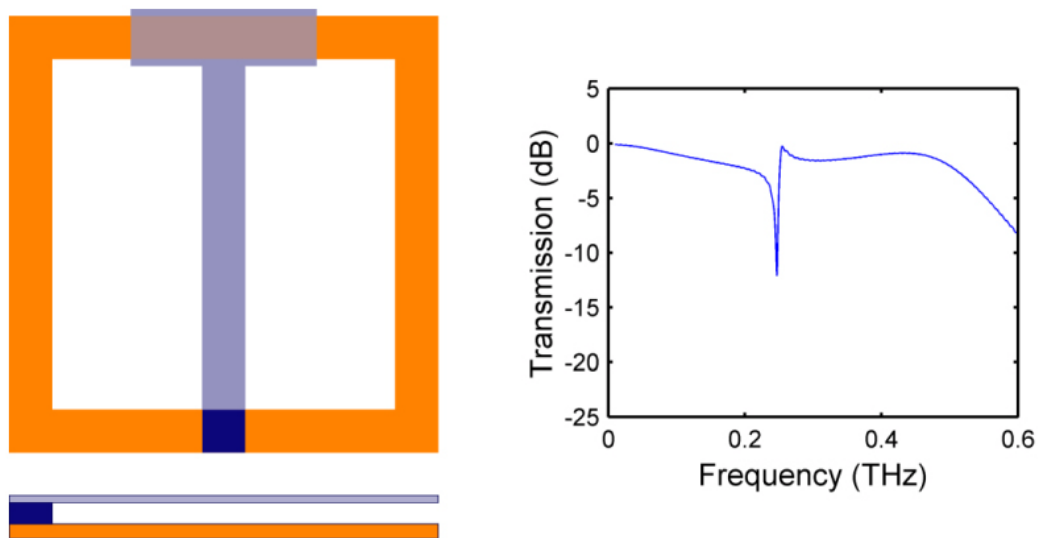


Fig. 1d. The structure and the transfer characteristics of an eSRR modified to incorporate a parallel plate capacitor on the top arm of the structure. For the device simulated the sides are  $120\ \mu\text{m}$ , the arms are  $10\ \mu\text{m}$ , the height of the top plate from the bottom plate is  $3\ \mu\text{m}$ , and the bottom plate is  $60 \times 4\ \mu\text{m}$  square.

#### 4. Mechanical analysis of beam bending

Magnetic actuation of MEMS cantilevers have been investigated theoretically and experimentally for application to microfluidic control systems and RF-MEMS switches [31–36]. The earlier works in the literature consider a flexible beam, appended by an inflexible

and magnetic material coated extension [32, 33]. For such a structure, an analytic formulation for the beam profile under magnetic field is accurate if the beam material stays in the linear elasticity regime and the beam bending is small. In the present work, we apply the results of [32] directly to the structure under consideration. Figure 2 shows a structure that has been modified from the asymmetric eSRR from Fig. 1d.

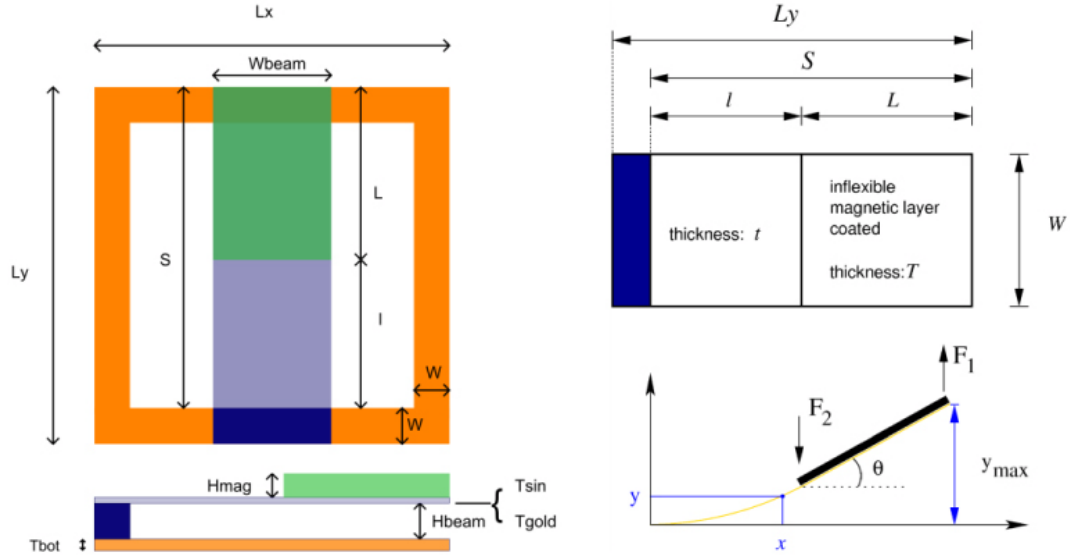


Fig. 2. The structure of the magnetically actuated eSRR with a flexing parallel plate capacitor. The relevant dimensions are labeled and are given in Table 2 for the three devices studied.

Figure 2 shows the forces that result from the magnetic field, which are generated if the easy magnetization axis of the thin magnetic film is perpendicular to the magnetic field. These forces generated by the magnetization of the coated inflexible magnetic layer results in a torque, which has the tendency to rotate this layer along the external magnetic field. For beam bending angles smaller than 25 degrees, the angular dependence of the forces can be ignored with at most 10% error in force calculation. Under high magnetic field conditions which result in the saturation of the magnetization, the resulting forces are calculated as:

$$F_1 = M_s W T H_1$$

$$F_2 = M_s W T H_2$$

where  $M_s$  is the saturation magnetization,  $W$  and  $T$  are the width and thickness of the magnetic layer and  $H_1$  and  $H_2$  are the magnetic field intensity at the two ends of the magnetic layer. For ease of calculation, the effect of force generated at the tip ( $F_1$ ) can be translated to the end of the flexible part of the cantilever. The result is a torque  $T_t$  given by

$$T_t = F_1 L$$

and a net force  $F$  given by  $F = F_1 - F_2$ . Assuming that the magnetic field will be uniform, the net force will be zero. Then, the flexible part of the beam will bend into a circular arc under the effect of the torque so that the beam will have a radius of curvature  $R$  and the tip of the flexible part will have an angle  $\theta$  which are given by;

$$\frac{1}{R} = \frac{T_i}{EI}$$

$$\theta = \frac{l}{R}$$

where  $I$  is the moment of inertia and  $E$  is the Young's modulus. By following the steps in [32], the maximum bending at the tip of the cantilever is found as:

$$y_m = R(1 - \cos(\theta)) + L \sin(\theta)$$

Since the angle  $\theta$  will be small for the application of interest, we can Taylor expand the above formula. With an expansion of up to and including second order terms and putting in the expression for  $\theta$  we have:

$$y_m = \frac{\theta^2 R}{2} + \theta L = \frac{l^2}{2R} + \frac{IL}{R}$$

The desired resonance frequency and the height set for flat position will determine the total length  $A$  of a side of the eSRR structure. Part of that length will have to be used to anchor the beam. Calling the remaining length as  $S$ , the flexible part will be  $l=(S-L)$  micrometer long. With this constraint we get:

$$y_m = \frac{(S-L)^2}{2R} + \frac{(S-L)L}{R}$$

The value of  $L$  that maximizes  $y_m$  can be found by replacing  $R$  with  $\frac{EI}{F_1 L}$  and equating the derivative of the above formula to 0 as:

$$L = \frac{S}{\sqrt{3}}$$

However, the design can utilize a length different than the value given above, in order to trade-off the magnetic field that needs to be applied versus the length and hence the stress of the flexible part of the cantilever.

The beam in Fig. 2 can be a composite structure of a layer of gold for low resistance and a mechanical support layer for ensuring the beam is stiff enough to hold the weight of the magnetic layer and also to avoid fabrication problems such as stiction. For the gold conduction layer, we employ a thickness of 0.2  $\mu\text{m}$  which is larger than one skin depth. For the mechanical support layer, a conventional choice is plasma chemical vapor deposited silicon nitride. In this work, we employ a 0.2  $\mu\text{m}$   $\text{Si}_3\text{N}_4$  support layer on top of the gold cantilever. The Young's modulus and yield strengths of gold and  $\text{Si}_3\text{N}_4$  are shown in Table 1. Keeping the cantilever thickness as small as possible is important to reduce the stress that results from bending. In the designs below, in order to compensate for the resistance of the thin gold layer in the cantilever, the cantilever structure is set to be as wide as the capacitive overlap region.

The power dissipation in the coil that will be used to generate the actuating magnetic field can be an important practical concern. The coil power dissipation and mechanical stability considerations dictate that it will be advantageous if the cantilever beam is anchored at a high position so that it lies in the middle of its range of movement at its flat position. However, this implies that the design procedure as described in the results section is more involved and this approach was not used in this work.

In order to safely stay in a range where the mechanical stability or the fabrication yield and reliability details will not undermine the relevance of the simulations performed, this work makes the assumption that the beam actuation will be limited to a maximum stress of 150 MPa and that the beam tip will not come closer than 0.4  $\mu\text{m}$  to the bottom conductor



surface. These assumptions limit the tuning range that can be demonstrated here but also mean that an experimental realization can be readily achieved. However, even with these constraining and conservative assumptions, a large tuning range can be achieved as shown below.

Table 2 provides the parameters used for the three tunable structures simulated in detail. Table 2 also provides the stress in the gold and the silicon nitride layers of the cantilever calculated at the maximum height of the cantilevers. The calculations were made using standard beam theory formulae [39]. It can be seen that the stress in the gold and silicon nitride film remains in the safe region.

**Table 1. Mechanical properties of the cantilever materials**

	Young's Modulus (GPa)	Yield Strength (GPa)	Ultimate Strength (GPa)
Gold [40]	80	0.15 to 0.30	0.3
Si <sub>3</sub> N <sub>4</sub> [40]	120	–	6

**Table 2. Dimensions, calculated beam stress and actuating field magnitude of the MEMS-SSR designs.**

Parameter	Design 1	Design 2	Design 3
L <sub>x</sub> , L <sub>y</sub> (μm)	240, 80	120, 80	130, 60
T <sub>bot</sub> (μm)	3	2	2
S, L, l (μm)	70, 40, 30	70, 40, 30	48, 16, 32
W <sub>beam</sub> (μm)	40	20	30
T <sub>gold</sub> , T <sub>sin</sub> (μm)	0.2, 0.2	0.2, 0.2	0.13, 0.13
H <sub>beam</sub> (μm)	0.4	1	0.4
H <sub>mag</sub> (μm)	5	5	5
Max displacement (μm)	12	12	12
Tuning range (THz)	0.147–0.275	0.323–0.471	0.265–0.514
Max stress in gold (MPa)	146	146	147
Max stress in SiN (MPa)	86	86	87
Magnetic field for max displacement (kA/m)	26	26	65
Periodicity in the x-direction (μm)	260	140	150
Periodicity in the y-direction (μm)	100	100	80

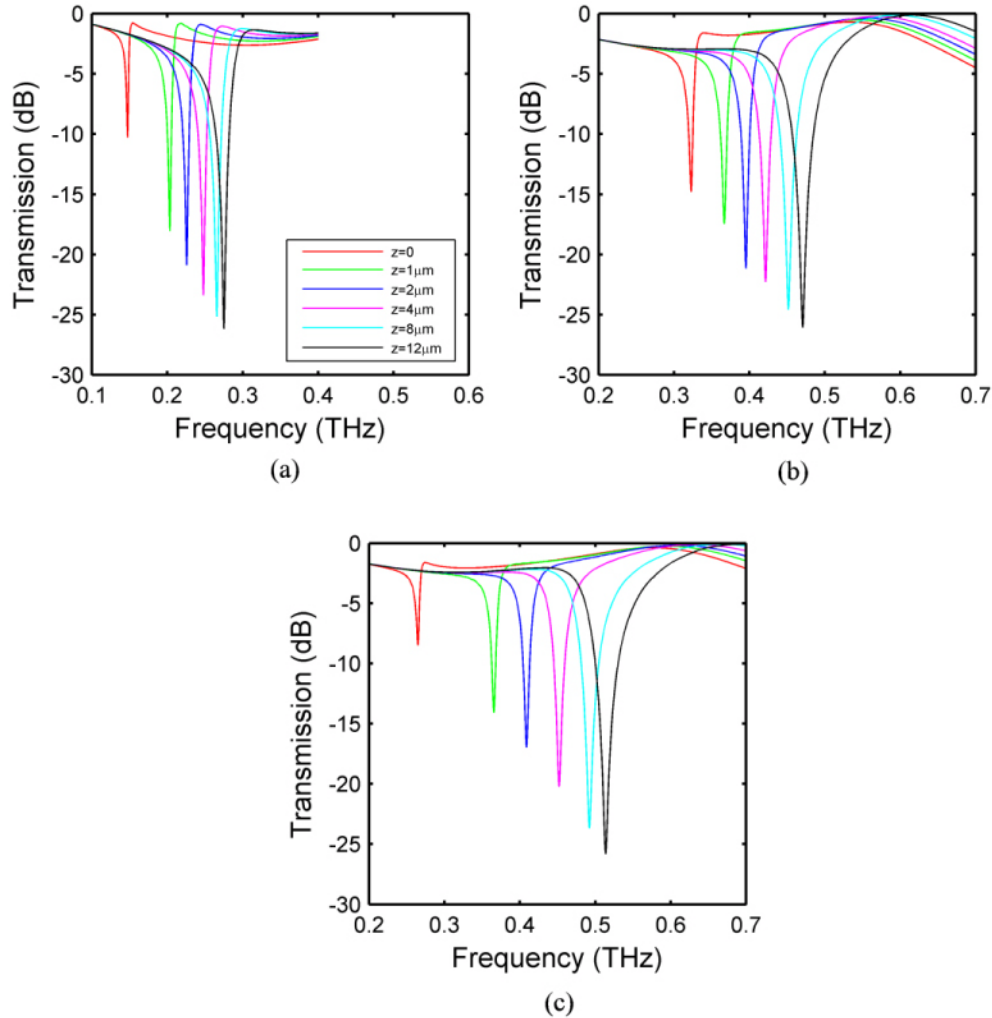


Fig. 3. Tuning characteristics of the three devices whose parameters are given in Table 2. a) Device 1, b) Device 2, c) Device 3.

## 5. Simulations and discussion

The beam profiles were calculated by using the methodology described in the previous section for the parameters shown in Table 2. The calculated beam profiles were then imported into CST simulator and used for generation of the eSRR structure by line sweep and sheet thickening operations. Figure 3 shows the transfer characteristics of several beam positions for the designs parameterized in Table 2. It can be seen that Design 1 has a tuning range of 0.147 to 0.275 THz and Design 2 has a tuning range of 0.265 to 0.514 THz.

The criterion in selecting these parameters was to obtain a transmission minimum less than  $-10$  dB at the low end of the frequency range. Since the minimum capacitance and the highest frequency that can be achieved is limited by the actuation range (maximum bending angle as dictated by stress limits), the frequency range obtainable is limited by the maximum capacitance that can be used at the low frequency region while the beam is flat or bent-down.

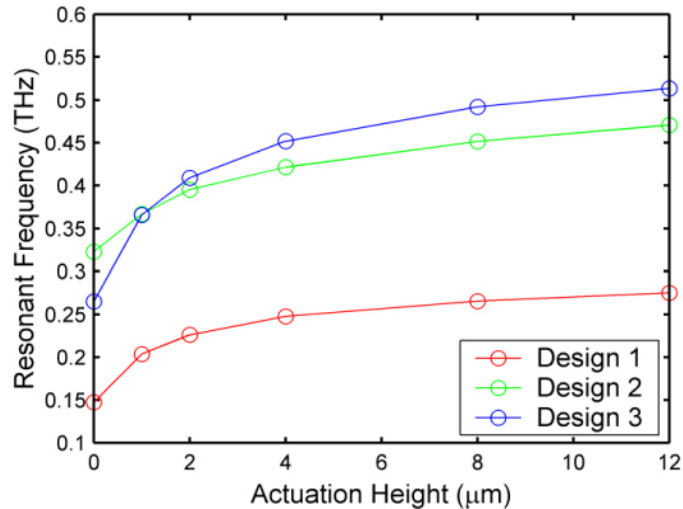


Fig. 4. Change of resonant frequency as a function of beam height for the simulated devices.

The working principle of the eSRR's can be modeled via a series RLC resonant circuit [41]. The data presented in Fig. 3, indicates that the bandwidth remains the same as the resonant frequency is varied by changing the capacitance. The constant bandwidth implies that the loss in the circuit is not changing. The variation observed in the transmission minima can be understood through considerations of the quality factor. An increase in the capacitance in a series RLC circuit implies a decrease in the quality factor. The change of the quality factor is related to the decrease of the resonance frequency while the bandwidth stays the same. This expected change in the quality factor is observed in Fig. 3.

With these observations, the design starts by implementation of an eSRR at the low end of the frequency range using the maximum capacitance possible while still maintaining a transmission minimum of less than  $-10$  dB. Then the higher end of the tuning range is determined by the stress limit of the material. The stress in the beam can be reduced by using a thinner cantilever, but since capacitance varies approximately inversely proportional to the spacing, the increase that can be achieved is limited. Figure 4 shows the change in the resonant frequency as a function of actuation height for Device 1. It can be seen that the increase of the resonant frequency slows down with increasing height as expected.

As the low end of the frequency range is increased, the inductance and the capacitance of the circuit must be decreased. The changes that can be made to reduce the capacitance or the inductance come at the expense of decreased tuning range. The capacitance can be decreased by using a narrower beam, but this increases the loss on the thin beam conductor. Alternatively, the capacitance can be decreased by increasing the beam height, but this limits the change in the capacitance and the change in the resonance frequency.

An alternative option that can be exercised to decrease the capacitance is to reduce the overlap of the cantilever with the top arm. Through this option the capacitance can be decreased to about  $\frac{1}{4}$  of the full coverage before the fringe capacitance starts to limit the variation that can be achieved by the actuation of the cantilever.

Design 3 is a structure that takes the above considerations into account and uses two nearly square inner loops ( $38 \mu\text{m}$  by  $36 \mu\text{m}$ ) and a reduced overlap structure. By employing numerous numerical simulations, we have observed that the square inner loops are optimal when both mechanical and electrical properties are taken into account. By this approach, the tuning range can be adjusted to cover the frequencies from 0.265 to 0.514 THz which is almost an octave. Hence, using the approaches described above, it is possible to increase the tuning range. It needs to be noted that in order to increase the operational frequency range, the dimensions of the structure, and in particular the height, is made smaller. The smaller structure height ( $L_y$  in Fig. 2) puts more stringent stress requirements on the beam and

ultimately limits the actuation that can be achieved. For Device 3, the thicknesses of the cantilever materials were decreased to 0.13  $\mu\text{m}$  in order to stay in the stress limit of gold. Furthermore, in order to limit the stress in the cantilever, the inflexible magnet part of the cantilever was shortened from the optimal 27  $\mu\text{m}$  to 16  $\mu\text{m}$ . This enabled a longer flexible region thus reducing the stress, but the magnetic field required for the actuation increased.

## **6. Conclusion**

The electric split-ring resonator structure has been modified to incorporate a cantilever beam. Tuning of the resonant frequency of the eSRR metamaterial by a magnetically actuated cantilever has been demonstrated using full-wave time-domain electromagnetic simulations. The calculations regarding the bending that can be achieved by a magnetic field demonstrates that for realistic device dimensions, magnetic layer thickness and magnetic field of the cantilever beam can be bent enough to affect a large tuning range. A tuning range close to an octave has been demonstrated for the low-end of the terahertz band. The width of the tuning range narrows down as the frequency is increased. The factors influencing the performance of the cantilever beam eSRR structures were discussed. The trade-offs involved in the design process indicate that the maximum operational frequency of the MEMS cantilever eSRR structures will depend on the properties of the cantilever and the magnet materials used to fabricate the structure.

## **Acknowledgements**

The authors acknowledge support from TUBITAK projects 108E123 and 109E001.